metals

MDPI

Article

Effects of PZT Reinforcement on the Properties of Fe-Based Composites Fabricated by Powder Metallurgy

Yousef Alshammari [1,2], Jafarali Parol [2], Fei Yang [1] and Leandro Bolzoni [1,*]

[1] School of Engineering, The University of Waikato, Private Bag 3105, Hamilton 3240, New Zealand
[2] Energy and Building Research Centre, Kuwait Institute for Scientific Research, P.O. Box 24885, Safat 13109, Kuwait
* Correspondence: leandro.bolzoni@waikato.ac.nz

Abstract

Fe composites are highly valued for their unique mechanical and magnetic properties, making them essential in various industrial applications. This study represents the first reported attempt to combine PZT into an Fe matrix, aiming to develop novel Fe-PZT composites. The primary objective was to assess how the concentration of PZT influences the properties of these composites. The results show that increasing the PZT content in Fe-xPZT composites (where x = 1, 5, and 10 wt.%) reduces the relative sintered density. Microstructural analysis reveals that the composites with higher PZT levels contained numerous large, irregularly shaped pores due to a pronounced Kirkendall effect and limited densification. Furthermore, the evaporation of the volatile PbO compound was observed to affect the thermal stability of the PZT system, leading to reduced composite homogeneity. SEM analysis showed the formation of intermetallic compounds corresponding to Fe_2Ti, FeTi, and $FeZr_2$. Finally, an increase in PZT content tends to degrade the tensile and mechanical properties of the Fe-xPZT composites, though they still do not fail catastrophically. These preliminary findings prove the concept of the feasibility of producing Fe-PZT composites and set the basis for the optimization of their manufacturing process. This should eventually unlock the possibility of producing multifunctional materials.

Keywords: iron composite; lead zirconate titanate; powder metallurgy; mechanical properties

Academic Editors: Magdalena Barbara Jabłońska, Grzegorz Korpala, Marek Wojtaszek, Marek Tkocz and Joanna Kulasa

Received: 12 January 2026
Revised: 31 January 2026
Accepted: 3 February 2026
Published: 5 February 2026

1. Introduction

Iron (Fe) is the third most abundant metal in the Earth's crust and is thus highly used in engineering applications, especially in the form of steel. While Fe exhibits versatile structural and magnetic properties, it still faces key challenges, for example, under high-temperature conditions. Promising solutions to these problems may be metal matrix composites (MMCs). They offer improved strength and Young modulus, control over the coefficient of thermal expansion, and excellent properties at high temperatures. Fe-based alloys reinforced with TiC particles have been employed for many years in a variety of industrial applications (e.g., tools, cutting blades, wear parts, and dies). Fe-TiC MMCs offer greater stiffness and wear resistance with lower density compared to unreinforced Fe [1]. Kim et al. [2] reported that increasing the reinforcement content in Fe-TiC MMCs leads to an increase in the compression yield stress of the composites. Wang et al. [3] fabricated Fe-matrix composites reinforced with SiC particles (3, 13, 21, 45 μm) using the hot-pressing sintering technique. The sample with a SiC particle size of 13 μm demonstrated the best combination of elongation and tensile strength. Chrysanthou et al. [4] successfully

developed MMCs with Fe as the metal matrix and (Ti, V)C as the reinforcement. The authors emphasized that an increase in the V content led to a refinement of the grain size of ferrites and carbides in the composite. This led to an increase in the microhardness. A study by Parswajinan et al. [5] focused on the fabrication of nano-ferrous composites reinforced with multi-walled carbon nanotubes (0.25, 0.5, and 0.67 wt.%) using the powder metallurgy (PM) technique. From these studies, it is inferred that Fe is commonly chosen as one of the materials for the metal matrix for a series of experiments to check the possibility of fabricating MMCs with a set of sufficiently high material properties. The key advantage of this element is its availability and low cost in comparison to other structural metals like Ti [6]. Therefore, the use of this metal as a matrix for MMCs significantly reduces the cost of raw materials and the resulting composite compared to other metal candidates. The processing of ferrous alloys and composites by the PM method is known in every detail, and a huge number of scientific publications are devoted to it.

Ceramic-based materials such as piezoceramics have also gained attention for their multifunctional properties. Piezoceramics have been widely used in several microelectronic and optoelectronic applications [7,8]. Lead zirconate titanate (PZT) is the most explored and commercialized material from piezoceramics for its high piezoelectric capability [9]. The use of PZT is focused on piezoelectric transducers, multilayer capacitors, and pyroelectric detectors [10,11], as well as the biomedical implant industry [12]. PZT has an ABO_3-type perovskite structure with Zr^{4+} and Ti^{4+} ions [13,14]. The literature shows that all the available studies focusing on creating PZT/metal combinations are limited to investigating PZT-based composites [15–18]. Specifically, a generally inert conductive metal like Ag or Pt is added as reinforcement to the PZT matrix [14]. The primary aim has been to increase the mechanical behavior, especially electrical fatigue, of the brittle PZT matrix. However, this has also led to significant unexpected improvement in the dielectric properties in the form of humongous dielectric constant values [19–23]. Conversely to the literature, our recent study reported improved mechanical properties in Ti-PZT composites at low PZT content, with degradation at higher levels due to porosity [24]. This study extends the investigation to Fe-PZT composites, which remain greatly unexplored in the literature. To the best knowledge of the authors, only the recent work of Yu et al. [25] considered the creation of Fe-PZT compositions. However, the study actually focused on functionally graded materials, aiming at tackling debonding and fracture problems caused by differences in thermal expansion coefficient.

The literature thus shows that, to date, the potential for developing novel multifunctional materials by combining the structural properties of Fe and the functional properties of PZT has not been considered. In particular, PZT-reinforced Fe-based composites might have autogenous sensing and damping capability on top of structural performance. Examples of potential applications include the self-monitoring and/or damage detection of structural engineering elements and energy harvesting devices. However, the practicality of the production of Fe-PZT composites starting from an intimate blending of the two components needs to be initially explored. Therefore, this preliminary study aims to study the feasibility of reinforcing Fe with low PZT contents (1, 5, and 10 wt.%). In order to assess such feasibility, we investigated how PZT affects the chemical, physical, and structural properties of the resulting composites. The insight gained set the foundation for the optimization of the manufacturing process, to then justify the quantification of functional properties in subsequent investigations. PM is routinely utilized as a fabrication process for both metals and piezoceramics, and several publications have successfully created Fe and PZT using PM individually. This can, consequently, be leveraged to define the experimental conditions of this initial work. Accordingly, the classical PM route of press and sinter was

selected in the investigation because it is the cheapest and most straightforward method to work with materials in powder form.

2. Materials and Methods

The starting materials included a water-atomized Fe powder with a particle size of 10 µm (Sigma Aldrich, Auckland, NZ) and a PZT powder (APC International, Campbell, CA, USA) supplied as 1.1 wt.% PVA-based binder agglomerates to be used as reinforcement (Figure 1).

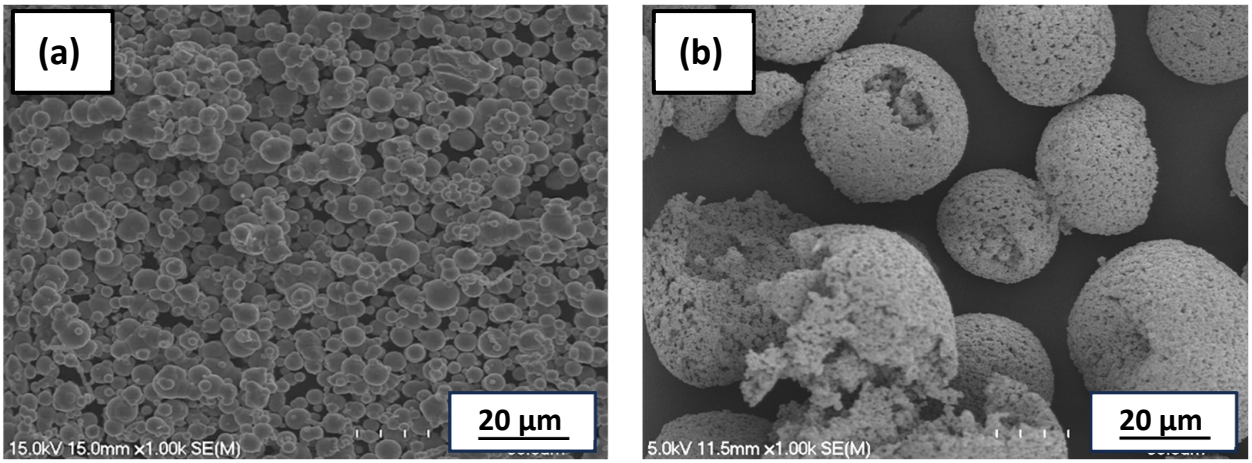

Figure 1. SEM micrographs of the particle morphology of the raw powders: (**a**) water-atomized Fe and (**b**) PZT.

The current study focused on Fe-xPZT composites, where the PZT content was 1, 5, and 10 wt.% and samples were labelled Fe-1PZT, Fe-5PZT, and Fe-10PZT, respectively. Firstly, the desired powder proportions were mixed in a V-blender operated at 45 rpm. The mixtures were then placed into a 40 mm die for their pressing at 200 °C by a 100-ton hydraulic press machine applying a uniaxial pressure of 600 MPa maintained for 10 s. The cylindrical Fe-xPZT green compacts were subsequently placed on a layer of loose PZT powder in an alumina crucible. The crucible was fully covered to minimize the volatilization of PbO [26]. Another layer of zirconia balls was placed on top of the PZT layer to avoid the possible reaction between the sample and the loose PZT powder. To sinter the green compacts, vacuum sintering (ZSJ—20 × 30 × 30, Advanced Corporation for Materials & Equipment's Co., Ltd., Changsha City, Hunan, China) using a vacuum level of about 10^{-2} Pa was employed. The sintering conditions of 1300 °C with a holding time of two hours were selected according to the literature for each individual element. In previous studies, these conditions ensured the consolidation of Fe-based and PZT-based green compacts [27,28]. For the first 500 °C, the samples experienced a heating rate of 2 °C per minute and the temperature was held for 30 min. This heating profile was designed to avoid any possible crack initiation due to the gas release that could happen during the binder-removing process. After that, the temperature was increased again to reach 1300 °C with a heating rate of 10 °C per minute.

The rule of mixtures was employed to calculate the theoretical density of the Fe-xPZT composites [29]. The principle of floating was applied [30] for measuring the sintered density. To determine the properties of the porosity, such as shape, size, and distribution, 15 images per sample were taken by means of an Olympus optical microscope (OM) (Olympus, Tokyo, Japan) with a digital Nikon camera (Nikon, Ltd., Tokyo, Japan) attached and analyzed via the ImageJ software 1.52. A Hitachi S-4700 scanning electron microscope (SEM) (Hitachi, Ltd., Tokyo, Japan) was utilized to examine the microstructural properties.

The metallographic preparation of the samples included mounting, grinding with SiC papers, and final polishing with a SiO_2-based solution. An X'Pert diffractometer (Philips, Amsterdam, Netherland) X-ray diffraction (XRD) with a Cu Kα radiation wavelength of 1.54 Å and a scan step size of 0.013° was employed to identify the resulting phases. The combination of thermal analysis and thermogravimetric analysis measurements was obtained in a single process using a 449 F5 Jupiter (NETZSCH, Selb, Germany) simultaneous thermal analyzer (STA). The thermal behavior was obtained for both raw powders and Fe-xPZT composites. Each powder was placed in an alumina crucible and heated up to 1300 °C with a heating rate of 10 °C per minute under Argon gas with a flow rate of 70 mL per minute. An Instron machine 33R4204 (Instron, Norwood, MA 02062, USA) with a crosshead speed of 0.1 mm/min was employed to evaluate the tensile behavior of the composites. The tensile samples had a dog-bone shape with a rectangular cross-section of 2×2 mm^2 and a gauge length of 20 mm. A minimum of three samples were tested to find the average values of ultimate tensile strength (UTS), yield stress (YS), and elongation (EL). The offset method was used to find the YS values of the tested samples. When needed, the dimensions of the samples were taken with a 2-digit digital caliper and the weight by means of a microbalance. The overall accuracy of the measurements and related standard deviation is, therefore, two decimals.

3. Results

The relative green and sintered density of the Fe-xPZT (x = 1, 5, and 10 wt.%) composites are summarized in Figure 2. A marked decrease in the sintered density of the studied samples is observed with an increase in the PZT content in the Fe matrix. The reduction in sintered density is most likely due to an increase in pore formation as a result of the Kirkendall effect with the increase in the PZT content, the volatilization of PbO from the surface of PZT, and the different starting values of the green density for composites with different ceramic content. For relative density values below 92%, it is expected that the irregularly shaped pores that were present in the compacts retain their irregular form after sintering.

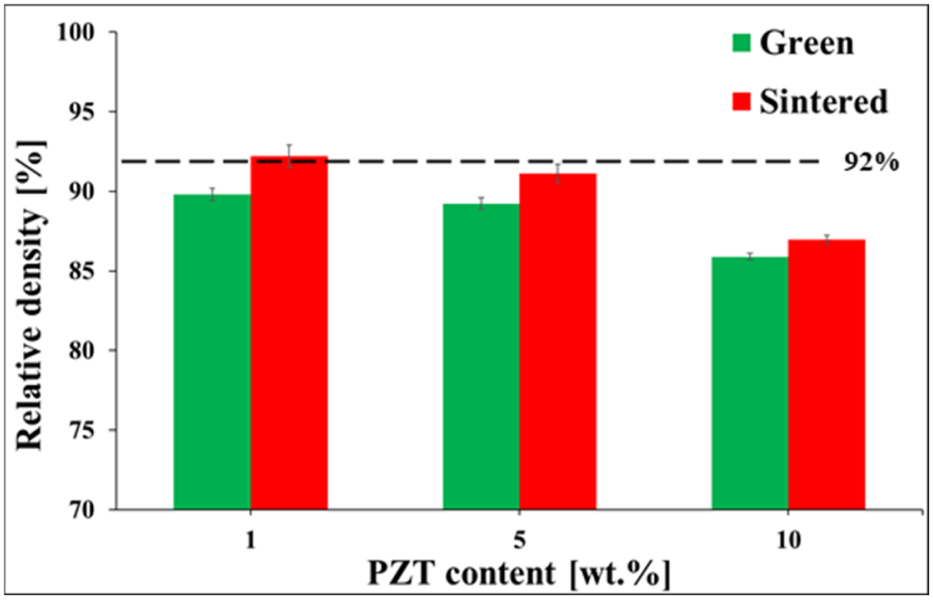

Figure 2. Variation in the green and sintered density of the Fe-xPZT composites vacuum sintered at 1300 °C.

The results of the OM analysis are presented in Figure 3, showing that an increase in the PZT content leads to the generation of a higher number of pores and areas where the Fe and PZT particles reacted.

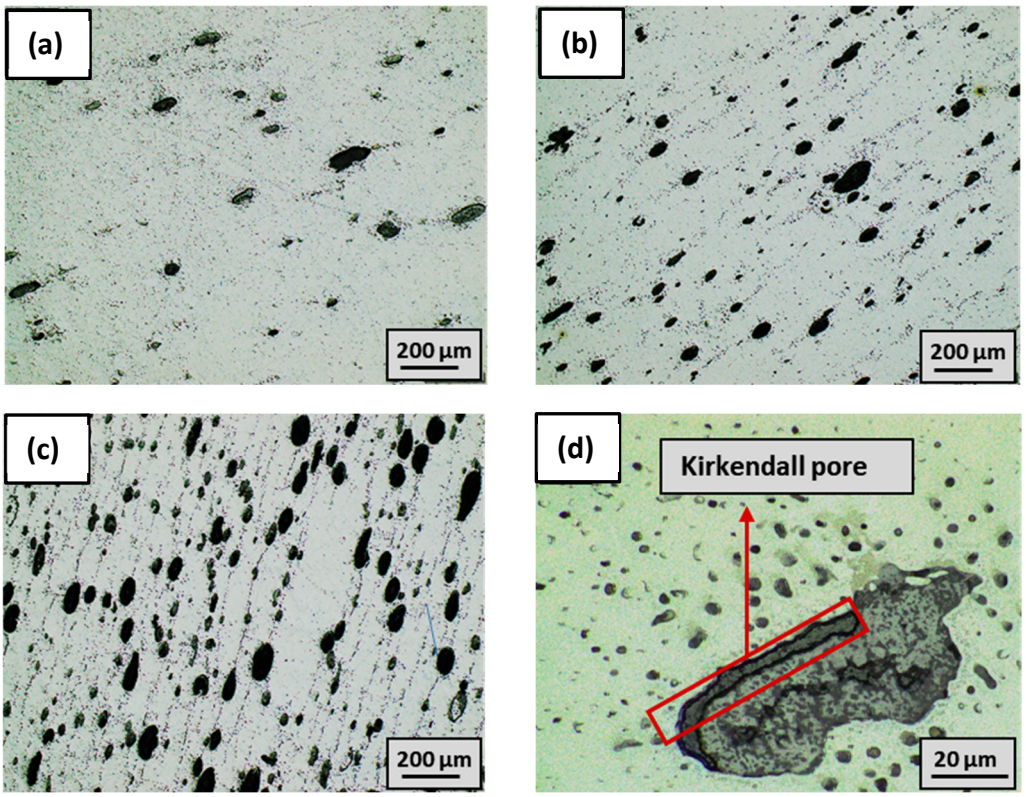

Figure 3. OM micrographs of the Fe-xPZT composites vacuum sintered at 1300 °C showing the distribution of the porosity: (**a**) Fe-1PZT, (**b**) Fe-5PZT, (**c**) Fe-10PZT, and (**d**) detail of a Kirkendall pore in the proximity of an undissolved PZT particle.

SEM backscatter analysis was used to clarify the nature of the reaction between Fe and PZT, and representative results are shown in Figure 4. At low magnification (Figure 4a), undissolved PZT particles are uniformly distributed throughout the microstructure. A closer analysis reveals the presence of different areas with significant differences in terms of chemistry (Figure 4b). Generally, Fe, Ti, and Zr are able to form a solution, while Pb is mainly found along the reacted area or as independent particles. From Figure 4c, the monotonic grey region (point 1) represents the Fe matrix with small quantities of diffused Zr atoms, most likely in the form of an Fe-Zr alloy. This occurs independently of the amount of PZT. At points 2, 3, and 4, rather high contents of Fe, Ti, and Zr are observed, which indicates the possible presence of intermetallic compounds of various compositions (Fe_2Ti and FeTi). At the same time, the presence of a relatively high oxygen content suggests the presence of $FeTiO_3$ and ZrO_2. Thus, the Laves phase FeTi in combination with ZrO_2 is likely to be present in the bright grey inclusions (point 2), whereas the combination of intermetallic Fe_2Ti and ZrO_2 is likely to be present in the dark grey area (Point 4). Point 3 is characterized by an excessive amount of Zr, probably indicating the presence of intermetallic compounds $FeZr_2$ in combination with Fe_2Ti and ZrO_2. The amount of these intermetallic compounds is progressively lower for lower additions of PZT. Point 5 likely corresponds to a droplet of liquid Pb formed as a result of the reduction reaction from PbO.

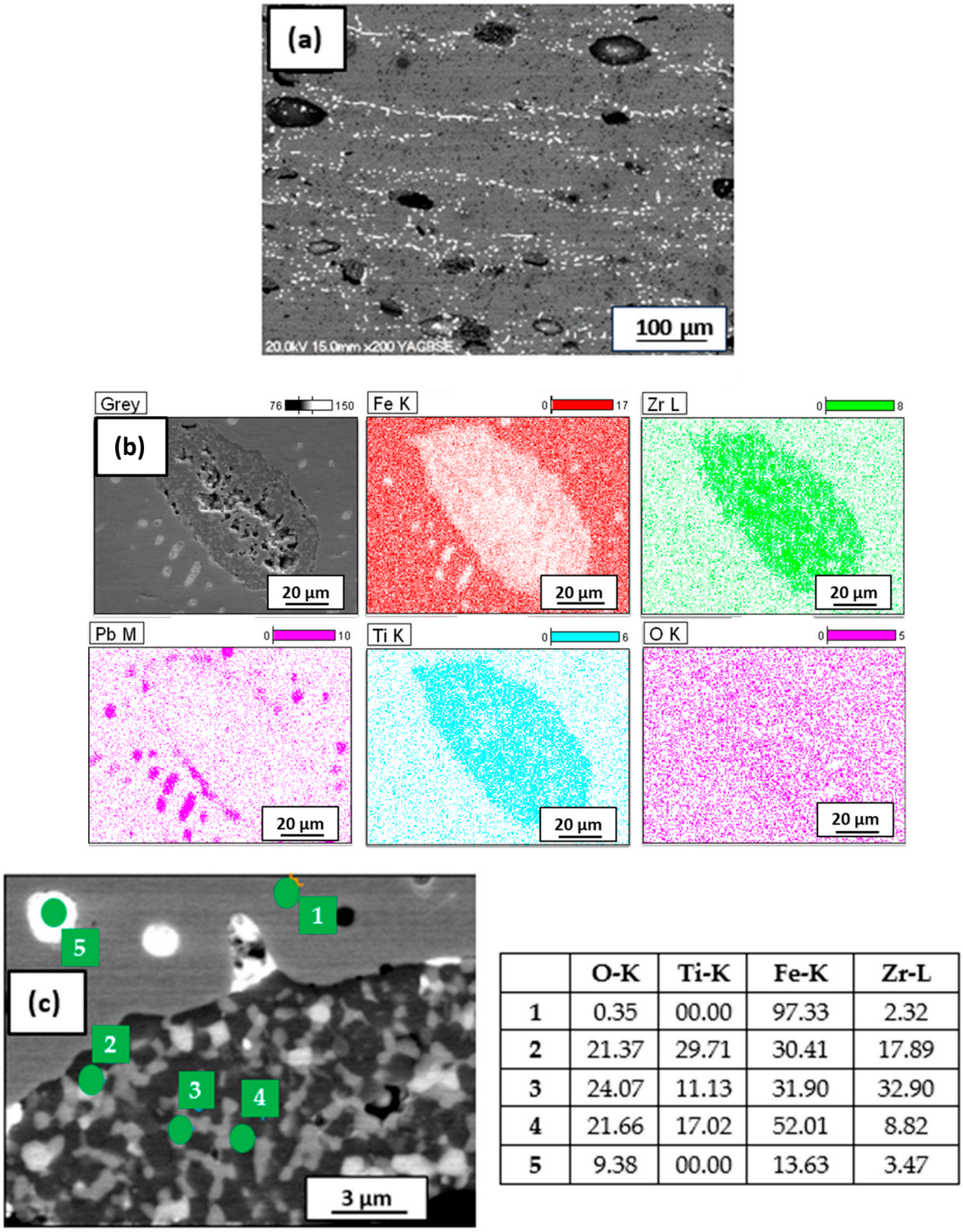

	O-K	Ti-K	Fe-K	Zr-L
1	0.35	00.00	97.33	2.32
2	21.37	29.71	30.41	17.89
3	24.07	11.13	31.90	32.90
4	21.66	17.02	52.01	8.82
5	9.38	00.00	13.63	3.47

Figure 4. SEM micrographs of the Fe-xPZT composites vacuum sintered at 1300 °C; (**a**) backscatter image showing the distribution of the undissolved PZT particles, (**b**) elemental maps showing the distribution of the elements around an undissolved PZT particle, and (**c**) high magnification backscatter image with point analysis (at.%).

The XRD patterns of the sintered Fe-xPZT composites are presented in Figure 5 along with that of pure PZT. In all the samples studied, only the α-Fe (bcc) phase is present as the metal matrix. The main peak of PZT becomes detectable only when the PZT content in the composites reaches 5 wt.%, whilst the presence of ZrO_2, PbO_2/Pb, and $FeTiO_3$ in the Fe-10PZT sample was also detected in the Fe-10PZT composites.

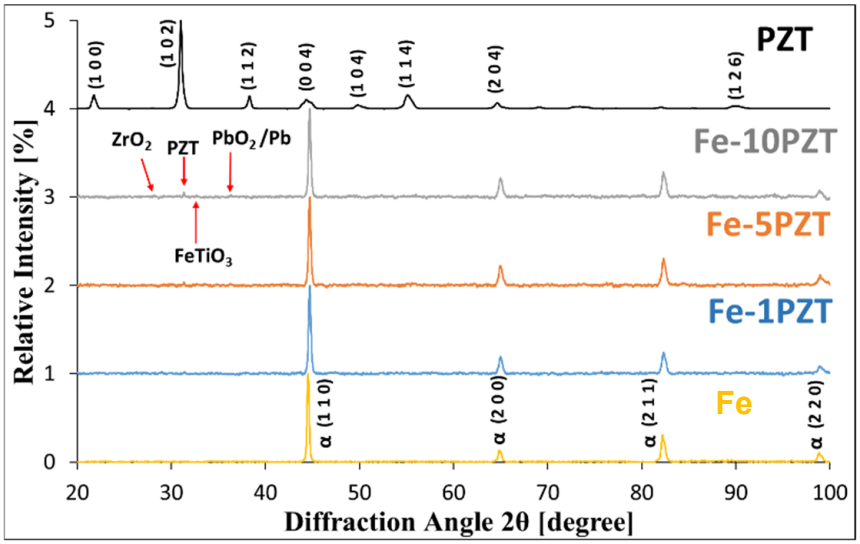

Figure 5. XRD patterns of the Fe-xPZT composites vacuum sintered at 1300 °C, along with those of the pure Fe and PZT powders.

The STA data for the pure powders and Fe-xPZT composites are presented in Figures 6 and 7. All the samples show a pronounced peak at temperatures below 100 °C (desorption and evaporation of moisture) during differential thermal analysis. Exothermic reactions associated with the burning of the PVA organic binder from the PZT are reflected in the broad peak in the temperature range from 280 °C to 400 °C. This peak is not present in the curve of the Fe powder, while the intensity of this peak in the curves of the powder blends is proportional to the PZT content. The following peak observed in the PZT curve is associated with the crystallization of the perovskite phase, occurring within the temperature range of 600 °C to 620 °C [31]. The peak at 770 °C, which is present on all curves of samples containing Fe, refers to the ferromagnetic–paramagnetic transition in α-Fe. The endothermic reaction at 920 °C corresponds to the α-γ phase transition, as detected in pure Fe, Fe-1PZT, Fe-5PZT, and Fe-10PZT. The curves of the Fe-xPZT powder blends display smooth peaks of reactions in the temperature range of about 1020 °C to 1120 °C. The higher the PZT content in the test powder mixture, the earlier the curve changes its character. This is related to the formation of intermetallic phases (Figure 4). The last significant region visible exclusively on the curve for PZT lies in the temperature range of about 1170 to 1230 °C. This peak reflects a phase transition in the high-temperature ZrO_2-TiO_2 phase [32].

The thermogravimetric curve of the pure PZT powder shows that the first significant weight reduction occurs in the temperature range of 270 to 420 °C (Figure 7). This is associated with the decomposition of organic components of the binder system. The formation of a PZT perovskite-type structure is reflected in the gradual weight loss. The next important peak is visible above 700 °C, sharply increasing after reaching a temperature of 950 °C, and is associated with the vaporization of PbO. The latter is also found in the Fe-xPZT composites, in which the lower the PZT content, the smaller the peak.

The tensile graphs of the Fe-xPZT composites (Figure 8a) indicate that all the Fe-containing specimens are characterized by both elastic and plastic regions. The plastic region is more dominant in samples with a lower PZT content. Figure 8b graphically represents the average UTS, YS, and EL values for each of the Fe-xPZT composites. The values of UTS, YS, and EL deteriorate with increasing ceramic content in the material from 210 MPa to 140 MPa, 122 MPa to 66 MPa, and 15% to 5%, respectively.

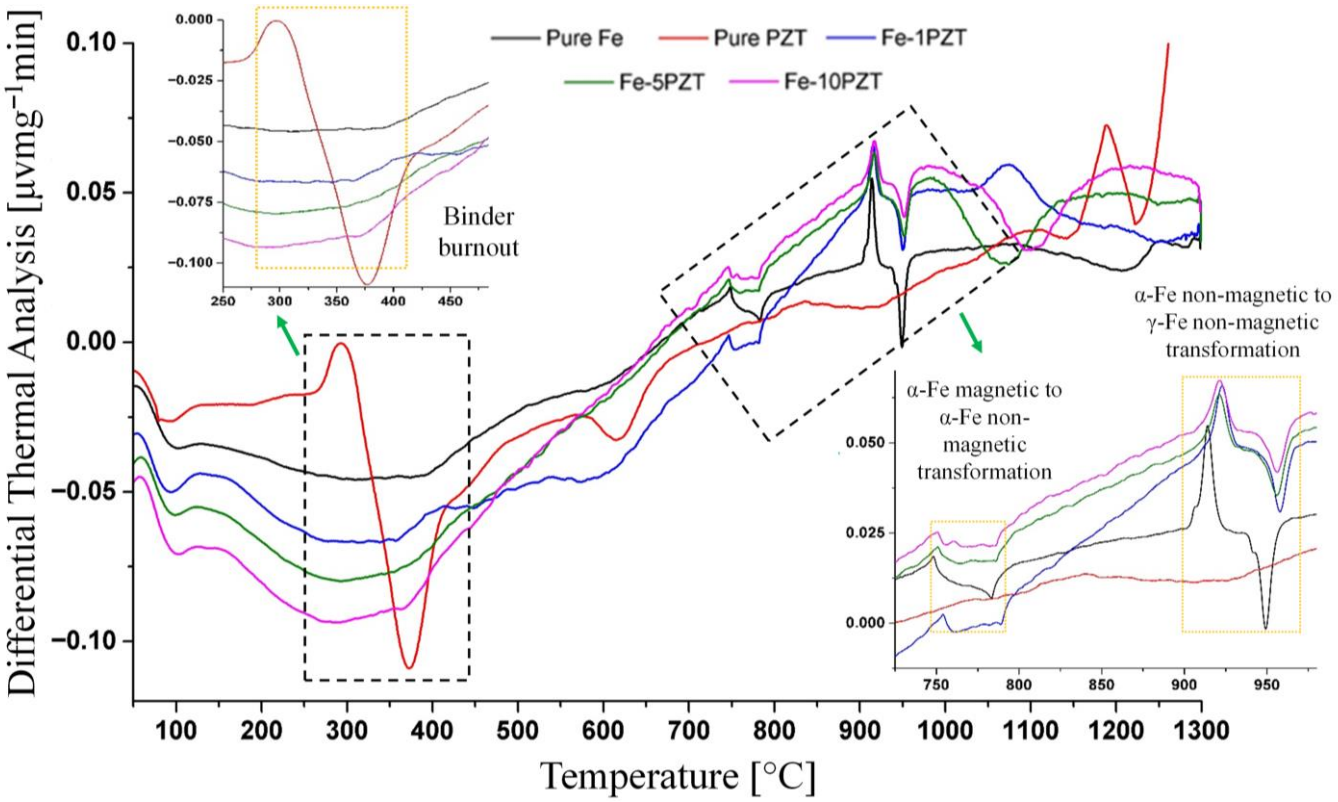

Figure 6. Results of the differential thermal analysis of the Fe-xPZT composites, along with those of the pure Fe and PZT powders.

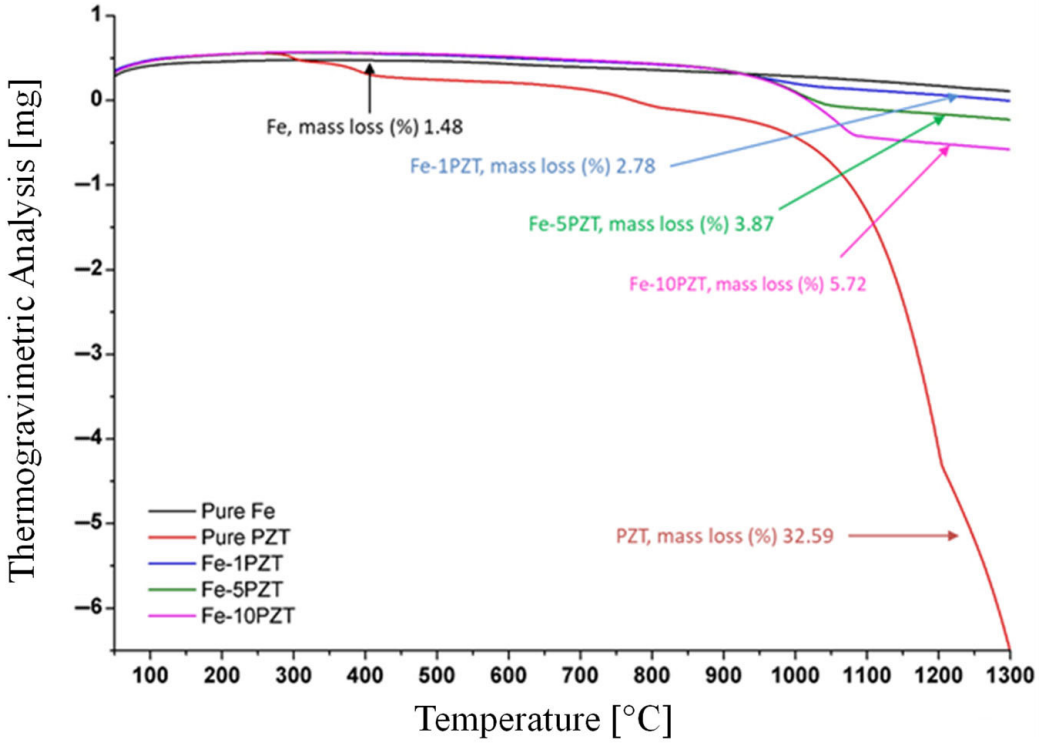

Figure 7. Results of the thermogravimetric analysis of the Fe-xPZT composites, along with those of the pure Fe and PZT powders.

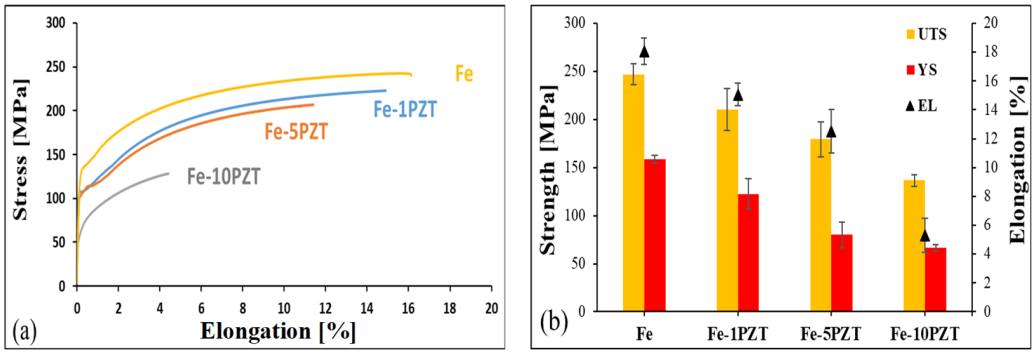

Figure 8. Tensile properties of the Fe-xPZT (x = 1, 5, 10 wt.%) composites vacuum sintered at 1300 °C: (**a**) representative stress versus strain graphs, and (**b**) average UTS, YS, and EL values.

4. Discussion

The results of the density measurements of the Fe-xPZT composites (Figure 2) show that the density values decrease with increasing PZT content. The composite samples with 5 wt.% and 10 wt.% PZT have relative sintered density values below 92%. The final stage of the sintering process, which includes the closure of irregular pores, corresponds to the sintering density of 92% of the theoretical density and higher [33]. Thus, in the Fe-5PZT and Fe-10PZT samples, irregular pores cannot effectively close and transform into smaller, rounded ones. The decrease in density of the composites is due to limited densification as well as increased pore formation as a result of the Kirkendall effect. Furthermore, the evaporation of PbO in PZT negatively affects the thermal stability of the system. This contributes to the deterioration of the sintered density with the PZT content. Nevertheless, a sufficiently high sintering temperature (1300 °C) and warm compaction (200 °C) provide satisfactory densities of both green compacts and sintered samples for their characterization.

Considering the diffusion rates of different metals in Fe and the self-diffusion rate of Fe, it is necessary to take into account the impact of phase transitions (one structural and one magnetic) that occur when Fe is heated from room temperature to 1300 °C. The self-diffusion data for Fe displayed in Figure 9 reveals that in the region of α-Fe, the Arrhenius plot shows a monotonic linear character as a result of the bcc crystal structure of α-Fe. However, the diffusion coefficient in the region of γ-Fe is significantly smaller due to its close-packed crystalline fcc structure. Consequently, the movement of both vacancies and Fe atoms is much more difficult compared to the bcc lattice.

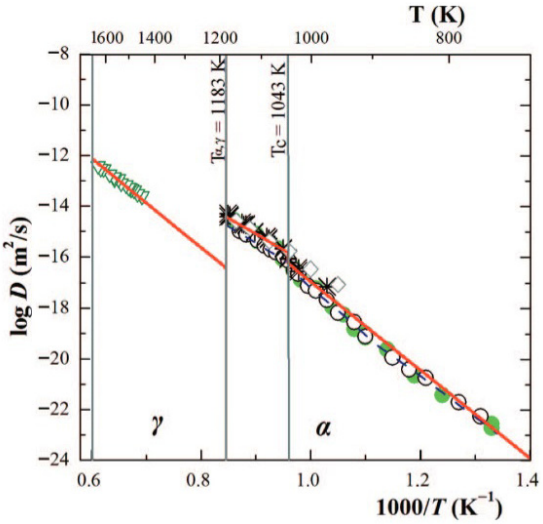

Figure 9. Self-diffusion data of Fe (adapted from [34,35]).

The sintering temperature of 1300 °C lies in the range of γ-Fe, which means lower values of the rate of self-diffusion of Fe. At the same temperature, Zr and Ti derived from the decomposition of PZT have significantly higher diffusion rates in Fe compared to the self-diffusion of γ-Fe. Diffusion parameters (activation energy E and diffusion coefficient D) for different substitutional elements in both α-Fe and γ-Fe are summarized in a study by Oikawa et al. [36]. As shown by Rusakov et al. [37], the diffusion of Fe in Zr ($D_{FeZr} = 3.5 \times 10^5$ μ^2/s) proceeds much faster compared to the diffusion of Zr in Fe ($D_{ZrFe} = 1.0 \times 10^4$ μ^2/s) at the same activation energy ($E = 2.0 \times 10^5$ J/mole).

The OM data (Figure 3) reveals the presence of round and irregular pores in all samples studied. Both the number of irregular pores and the pore sizes increase with the addition of the ceramic phase. In the Fe-10PZT samples, predominantly irregular pores are visible. As mentioned, the prevalence of irregular pores can be explained by insufficient densification of the Fe-5PZT and Fe-10PZT samples (below 92%, see Figure 2) and the manifestation of the Kirkendall effect. This behavior is not characteristic of other Fe–ceramic composites described in the literature that employ different types of ceramic reinforcements. For example, Li et al. [38] studied Fe matrix composites reinforced by different types of ceramic phases (SiC, Cr_3C_2, TiC, and Ti(C, N)) with a ceramic content of 5, 10, and 15 vol.% fabricated by PM using a traditional hot-pressing furnace. The results of optical microscopy showed that the samples with a low volume fraction (5 and 10 vol.%) of SiC and Ti (C, N) are characterized by a uniform distribution of the ceramic phase in the Fe matrix. Conversely, the Fe–ceramic composites with a volume fraction of 15 vol.% are characterized by an uneven distribution of these particles and the formation of clusters.

The results of the SEM analysis of the sintered Fe-xPZT samples (Figure 4) reveal that the addition of PZT reinforcements has a significant impact on the microstructural features of the Fe-xPZT composites. Specifically, particles of PZT tend to remain mainly along grain boundaries. In samples with high PZT contents, this phenomenon is most pronounced. According to the results of the elemental analysis, bright areas can be identified as droplets of liquid Pb formed as a result of the evaporation of PbO from PZT [39]. The resulting oxides of Fe and Zr are present as impurities in the Pb phase. The large grey areas represent the Fe matrix contaminated by small amounts of Zr.

Several phases were identified through point analysis of the Fe-5PZT and Fe-10PZT samples, which indicate the formation of intermetallic compounds. Intermetallics existing in the binary systems Fe-Ti and Fe-Zr are described in detail in [40,41]. The data obtained indicates that the existence of intermetallic compounds of the Ti-Fe system (FeTi and Fe_2Ti) is highly likely at the boundary of the reaction zone between the Fe matrix and PZT ceramics. Moreover, the presence of cubic intermetallic compounds c-$FeZr_2$ in the Fe-10PZT sample is expected. The obtained SEM data does not completely eliminate the possibility of the presence of the $Fe_{23}Zr_6$ phase at the grain boundaries. As evidenced by several theoretical and experimental studies, of all Fe-Zr intermetallics, $Fe_{23}Zr_6$ has the least ductile, elastic, and electronic properties. The literature notes that the only way to stabilize the $Fe_{23}Zr_6$ phase is with the presence of contaminations from the material of the crucible or impurities, for example, oxygen [42]. Otherwise, this intermetallic exists as the equilibrium phase with $FeZr_2$. Liu et al. [43] proposed that the $Fe_{23}Zr_6$ phase is formed as a result of the following peritectoid reaction: α-Fe + $Fe_2Zr \rightarrow Fe_{23}Zr_6$. Zhou et al. [44] noted that Zr and Ti, both of which are elements of the IV B group, can substitute for each other within limits in the binary compounds Fe-Zr and Fe-Ti. The tentative isothermal section of the tertiary Fe-Ti-Zr system (at 750 °C) is shown in Figure 10.

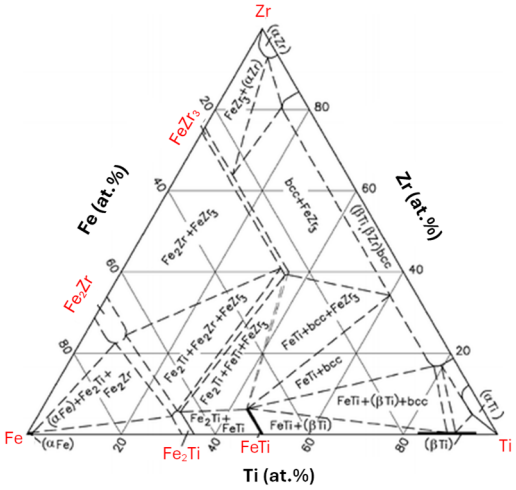

Figure 10. Fe-Ti-Zr tentative isothermal 750 °C section (adapted from [40]).

In the XRD patterns of the sintered Fe-xPZT samples (Figure 5), the crystalline peaks identify ferrite (α-Fe phase) as the only phase present in all three samples. The main peak of PZT is found in the Fe-5PZT and Fe-10PZT samples. The Fe-10PZT sample also contains ZrO_2, PbO_2, and $FeTiO_3$. The presence of ZrO_2 on the XRD pattern is consistent with the data obtained by point analysis. However, the other intermetallic phases are not detected as their amount is below the detection limit of the instrument.

From the STA analysis (Figures 6 and 7), several events are present in the curves, these include the following peaks: the desorption and evaporation of moisture (T < 100 °C curve); the decomposition and burning of organic components of the binder system (T = 280 to 400 °C); the crystallization of the PZT perovskite phase (T = 600 °C to 620 °C); the vaporization of excess PbO (T = 700 °C to 800 °C); and endothermic reactions in PZT associated with phase transition in the high-temperature ZrO_2-TiO_2 phase (T = 1170 °C to 1230 °C). The temperature of the ferromagnetic–paramagnetic transition in α-Fe (T~770 °C) corresponds to the data presented in a study by Arajs and Colvin [45]. The temperature for the α-γ transformation between the magnetic α phase and the paramagnetic γ phase in Fe (T~920 °C) is consistent with the data presented in a study by Maruno et al. [46]. The behavior seen in all the differential thermal analysis curves for the Fe-xPZT composites in the temperature range of about 1020 °C to 1120 °C reflects the formation of Fe_2Ti and FeTi intermetallic phases that can exist in the system. As reported in the phase diagram of Fe-Ti [41,47], the Laves phases belonging to both types may exist in this temperature range. A third suggested intermetallic compound ($FeZr_2$) exists at lower temperatures of up to 974 °C.

The results of the tensile tests (Figure 8) show that all the studied Fe-xPZT samples exhibit both plastic and elastic deformations. In general, a trend towards a deterioration of tensile properties with an increase in PZT is evident. Adding 1 wt.% PZT to the Fe matrix markedly degrades the UTS, YS, and EL to 210 MPa, 122 MPa, and 15% compared to 247 MPa, 158 MPa, and 18% of that of pure Fe powder. The effect of the ceramic content on the tensile properties of the resulting composites largely depends on the nature of the selected reinforcement. Although the PZT used as a ceramic reinforcement exhibits relatively high YS, its tensile strength is still much lower than that of metals. This explains the observed deterioration in the tensile properties of Fe-xPZT composites with increasing ceramic content. Moreover, the high porosity and the presence of intermetallic compounds (Fe_2Ti, FeTi, $FeZr_2$) negatively affect the tensile properties, facilitating crack formation in the PZT clusters, as seen in Figure 11. A greater amount of porosity provides an easy crack propagation pathway, which also contributes to the reduction in the tensile properties.

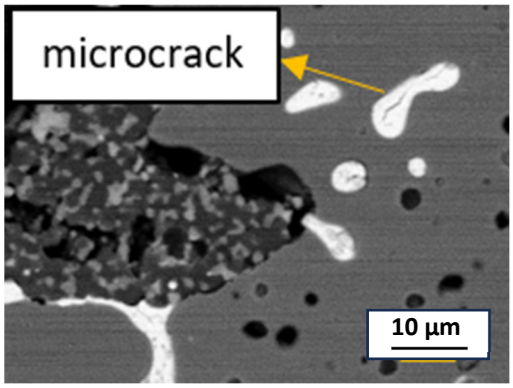

Figure 11. SEM micrograph showing a microcrack in the PZT cluster.

The tensile behavior found is consistent with the observations of other authors. Cao et al. [48] studied the mechanical properties of Fe–ceramic composites reinforced by a wide range of different ceramic phases. This includes TiC, SiC, TiN, and hybrid mixtures SiC + TiN, TiC + TiN, and SiC + TiC. For all the resultant composites, an increase in the ceramic content led to a significant decrease in the tensile strength. Li et al. [38] reported that out of different types of ceramic phases (SiC, Cr_3C_2, TiC, and Ti(C, N)) investigated as the reinforcing particles for the Fe matrix, the SiC particles have the most substantial effect on the YS of the final composite material. The best tensile properties of all the Fe–ceramic composites were measured for samples with a reinforcement content of 10 vol.%. Further addition of the ceramic phase led to a deterioration in tensile properties, which the authors attributed to the presence of microvoids in the samples at the high-volume fraction (15 vol.%). Instead of yielding, these microvoids lead to fracture, consequently leading to a sharp drop in strength.

This preliminary study about the production of Fe-xPZT composites proves that PM can effectively be used, though further optimization is needed. As pressure-assisted methods characterized by shorter processing time, hot-pressing or spark plasma sintering could be used to simultaneously reduce the amount of porosity and limit PbO evaporation. The incorporation of a sintering aid could also be considered to reduce the sintering temperature, though that would also change the reactivity of the material, the resulting microstructural features, and the final performance. The findings of this study primarily show that the relative density decreases, and the amount of reacted zone increases, with the PZT content. The presence of both a greater number of pores and intermetallic compounds reduces the tensile properties. Despite that, the Fe-xPZT composites never fail catastrophically, maintaining the ability to plastically deform when performing structurally. This means that the amount of PZT could be selected on the basis of the tensile properties required by the specific application. These pilot data set the foundation to conduct further development of Fe-xPZT composites, in which it would be justified to quantify functional properties like their piezoelectric and electromechanical behavior. If the latter are adequate, Fe-xPZT composites could be used in structural engineering elements with added self-monitoring and/or energy harvesting capabilities.

5. Conclusions

The study aimed at exploring the effects brought about by using PZT as a reinforcement in an Fe-based matrix to create Fe-PZT composites. The experimental data indicate that an increase in the ceramic content in the studied Fe-xPZT (x = 1, 5, 10 wt.%) composites has a significant effect on the relative sintered density, leading to its decrease. As evidenced by the OM data, samples with higher ceramic content demonstrate the presence of a significant number of larger pores of irregular shape due to insufficient densification

during high temperature sintering as well as the manifestation of the Kirkendall effect. The evaporation of the highly volatile PbO is a crucial factor that weakens the thermal stability of the PZT system and reduces the homogeneity of the composites. SEM micrographs suggest the formation of intermetallic compounds like Fe_2Ti, FeTi, and $FeZr_2$. A trend towards the deterioration of the tensile and mechanical properties with the increase in the PZT content is therefore observed. Nevertheless, the Fe-xPZT composites never fail catastrophically, proving their structural integrity. In the current study, the Fe-1PZT is the most promising in terms of the strength/elongation pair. The tensile response can then be tailored as a function of the PZT content for specific applications. By proving the concept, this study paves the way forward to optimizing the composition and manufacturing of Fe-PZT composites. They could eventually be used for structural health monitoring.

Author Contributions: Conceptualization, Y.A. and L.B.; methodology, Y.A., J.P., F.Y. and L.B.; validation, Y.A., J.P., F.Y. and L.B.; formal analysis, Y.A., J.P., F.Y. and L.B.; investigation, Y.A.; resources, L.B.; data curation, Y.A., J.P., F.Y. and L.B.; writing—original draft preparation, Y.A., J.P., F.Y. and L.B.; writing—review and editing, Y.A. and L.B.; visualization, Y.A., J.P. and L.B.; supervision, F.Y. and L.B.; project administration, L.B.; funding acquisition, L.B. All authors have read and agreed to the published version of the manuscript.

Funding: This research was partially funded by the New Zealand Health Research Council, grant number HRC 17-625 Explorer Grant.

Data Availability Statement: The original contributions presented in this study are included in the article. Further inquiries can be directed to the corresponding author.

Acknowledgments: The authors wish to acknowledge the support of the Kuwait Foundation for the Advancement of Sciences (KFAS).

Conflicts of Interest: The authors declare no conflicts of interest.

References

1. Zweben, C. Composite materials. In *Mechanical Engineers' Handbook, Volume 1: Materials and Engineering Mechanics*; John Wiley & Sons: Hoboken, NJ, USA, 2015.
2. Kim, J.M.; Park, J.S.; Yun, H.S. Microstructure and mechanical properties of TiC nanoparticle-reinforced iron-matrix composites. *Strength Mater.* **2014**, *46*, 177–182. [CrossRef]
3. Wang, Y.; Zhang, C.; Zong, Y.; Yang, H. Experimental and simulation studies of particle size effects on tensile deformation behavior of iron matrix composites. *Adv. Compos. Mater.* **2013**, *22*, 299–310. [CrossRef]
4. Chrysanthou, A.; Modi, O.P.; Han, L.; Ramakrishnan, N.; O'sUllivan, J.M. Formation and microstructure of (Ti, V) C-reinforced iron-matrix composites using self-propagating high-temperature synthesis. *Int. J. Mater. Res.* **2008**, *99*, 281–286. [CrossRef]
5. Parswajinan, C.; Ramnath, B.V.; Elanchezhian, C.; Pragadeesh, S.; Ramkishore, P.; Sabarish, V. Investigation on mechanical properties of nano ferrous composite. *Procedia Eng.* **2014**, *97*, 513–521. [CrossRef]
6. Bolzoni, L.; Esteban, P.; Ruiz-Navas, E.; Gordo, E. Mechanical Behaviour of Pressed and Sintered Titanium Alloys Obtained from Prealloyed and Blended Elemental Powders. *J. Mech. Behav. Biomed. Mater.* **2012**, *14*, 29–38. [CrossRef]
7. Kenji, U. Glory of piezoelectric perovskites. *Sci. Technol. Adv. Mater.* **2015**, *16*, 046001. [CrossRef]
8. Chen, C.; Wang, X.; Wang, Y.; Yang, D.; Yao, F.; Zhang, W.; Wang, B.; Sewvandi, G.A.; Yang, D.; Hu, D. Additive Manufacturing of Piezoelectric Materials. *Adv. Funct. Mater.* **2020**, *30*, 2005141. [CrossRef]
9. Park, J.; Lee, D.-G.; Hur, S.; Baik, J.M.; Kim, H.S.; Song, H.-C. A Review on Recent Advances in Piezoelectric Ceramic 3D Printing. *Actuators* **2023**, *12*, 177. [CrossRef]
10. Oliveira, C.; Longo, E.; Varela, J.; Zaghete, M. Synthesis and characterization of lead zirconate titanate (PZT) obtained by two chemical methods. *Ceram. Int.* **2014**, *40*, 1717–1722. [CrossRef]
11. Lay, R.; Deijs, G.S.; Malmström, J. The intrinsic piezoelectric properties of materials—A review with a focus on biological materials. *RSC Adv.* **2021**, *11*, 30657–33073. [CrossRef] [PubMed]
12. Goetzinger, N.C.; Tobaben, E.J.; Domann, J.P.; Arnold, P.M.; Friis, E.A. Composite piezoelectric spinal fusion implant: Effects of stacked generators. *J. Biomed. Mater. Res. Part B Appl. Biomater.* **2016**, *104*, 158–164. [CrossRef]
13. Bogdanov, A.I.; Mysovsky, A.S.; Kimmel, A.V. Theoretical study of the structure of lead zirconate-titanate $PbZr_{0.6}Ti_{0.4}O_3$. *Bull. Russ. Acad. Sci. Phys.* **2017**, *81*, 1075–1079. [CrossRef]

14. Bolzoni, L. Structural electroactive cermets: Dielectric and structural properties of conductive metallic reinforced piezoelectric ceramics. *Crit. Rev. Solid State Mater. Sci.* **2021**, *46*, 38–81. [CrossRef]
15. Takagi, K.; Li, J.-F.; Yokoyama, S.; Watanabe, R. Fabrication and evaluation of PZT/Pt piezoelectric composites and functionally graded actuators. *J. Eur. Ceram. Soc.* **2003**, *23*, 1577–1583. [CrossRef]
16. Fang, M.H.; Pan, W.; Wang, R.G.; Cao, Z.Z.; Chen, J.; Hou, L.K. Fabrication of Cu/PZT Functionally Graded Actuators by Spark Plasma Sintering. *Mater. Sci. Forum* **2003**, *423–425*, 423–426. [CrossRef]
17. Zhang, H.; Li, J.; Zhang, B. Sintering and Piezoelectric Properties of Co-Fired Lead Zirconate Titanate/Ag Composites. *J. Am. Ceram. Soc.* **2006**, *89*, 1300–1307. [CrossRef]
18. Xiang, P.; Dong, X.; Feng, C.; Liang, A.; Wang, Y. Dielectric Behavior of Lead Zirconate Titanate/Silver Composites. *Mat. Chem. Phys.* **2006**, *97*, 410–414. [CrossRef]
19. Hwang, H.J.; Watari, K.; Sando, M.; Toriyama, M.; Niihara, K. Low-Temperature Sintering and High-Strength Pb(Zr,Ti)O_3-Matrix Composites Incorporating Silver Particles. *J. Am. Ceram. Soc.* **1997**, *80*, 791–793. [CrossRef]
20. Zhang, H.L.; Li, J.F. Fabrication and Evaluation of PZT/Ag Piezoelectric Composites and Graded Actuator. *Key Eng. Mater.* **2004**, *280–283*, 1913–1916.
21. Pearce, D.H.; Button, T.W. Processing and properties of silver/PZT composites. *Ferroelectrics* **1999**, *228*, 91–98. [CrossRef]
22. Panteny, S.; Bowen, C.R.; Stevens, R. Characterisation of Barium Titanate-silver Composites Part II: Electrical Properties. *J. Mater. Sci.* **2006**, *41*, 3845–3851. [CrossRef]
23. Chen, C.Y.; Tuan, W.H. Mechanical and Dielectric Properties of $BaTiO_3$/Ag Composites. *J. Mater. Sci. Lett.* **1999**, *18*, 353–354. [CrossRef]
24. Alshammari, Y.; Yang, F.; Bolzoni, L. Quantification of the physical, microstructural, thermal, and mechanical properties of PZT-reinforced Ti-based composites. *J. Alloys Compd.* **2024**, *1000*, 175044. [CrossRef]
25. Yu, J.; Wang, Z.; Zhang, B.; Zhang, X.; Li, M. Fabrication of the Fe/PZT Functionally Graded Material and its Application on the Thermal Match for Transducers. *Mater. Sci.* **2022**, *28*, 178–183. [CrossRef]
26. Safar, M.; Button, T.W.; Zabcik, M. Control of PbO loss during sintering of PZT: Laboratory vs industry. In *2017 Joint IEEE International Symposium on the Applications of Ferroelectric (ISAF)/International Workshop on Acoustic Transduction Materials and Devices (IWATMD)/Piezoresponse Force Microscopy (PFM)*; IEEE: New York, NY, USA, 2017.
27. Gordo Odériz, E.; Gómez, B.; González, R.; Ruiz-Navas, E.M. Study for the Development of Fe-NbC Composites by Advanced PM Techniques. *Mater. Sci. Forum* **2007**, *534–536*, 637–640. [CrossRef]
28. Choi, Y.M.; Lee, Y.L.; Lim, E.S.; Trimzi, M.A.; Hwangbo, S.A.; Ham, Y.B. Performance Improvement of Ring-Type PZT Ceramics for Ultrasonic Dispersion System. *Micromachines* **2020**, *11*, 144. [CrossRef] [PubMed]
29. Bolzoni, L.; Ruiz-Navas, E.; Neubauer, E.; Gordo, E. Mechanical Properties and Microstructural Evolution of Vacuum Hot-pressed Titanium and Ti-6Al-7Nb Alloy. *J. Mech. Behav. Biomed. Mater.* **2012**, *9*, 91–99. [CrossRef]
30. Jia, M.T.; Gabbitas, B.; Bolzoni, L. Evaluation of Reactive Induction Sintering as a Manufacturing Route for Blended Elemental Ti-5Al-2.5Fe Alloy. *J. Mater. Process. Technol.* **2018**, *255*, 611–620. [CrossRef]
31. Bel-Hadj-Tahar, R.; Abboud, M.; Bouzitoun, M. Thermal analysis of the crystallization kinetics of lead zirconate titanate powders prepared via sol-gel route. *J. Therm. Anal. Calorim.* **2020**, *144*, 127–138. [CrossRef]
32. Troitzsch, U.; Ellis, D. The ZrO_2-TiO_2 phase diagram. *J. Mater. Sci.* **2005**, *40*, 4571–4577. [CrossRef]
33. Bolzoni, L.; Ruiz-Navas, E.; Gordo, E. Influence of Vacuum Hot-pressing Temperature on the Microstructure and Mechanical Properties of Ti-3Al-2.5V Alloy Obtained by Blended Elemental and Master Alloy Addition Powders. *Mater. Chem. Phys.* **2012**, *137*, 608–616. [CrossRef]
34. Mehrer, H. *Diffusion in Solids: Fundamentals, Methods, Materials, Diffusion-Controlled Processes*; Springer Science & Business Media: Berlin, Germany, 2007.
35. Zhang, B. Calculation of self-diffusion coefficients in iron. *AIP Adv.* **2014**, *4*, 017128. [CrossRef]
36. Oikawa, H. Review on lattice diffusion of substitutional impurities in iron. A summary report. *Technol. Rep. Tohoku Univ.* **1982**, *47*, 215.
37. Rusakov, V.S.; Sukhorukov, I.A.; Zhankadamova, A.M.; Kadyrzhanov, K.K. Simulation of diffusion and phase formation during isothermal annealing of lamellar Fe-Zr systems. *Mosc. Univ. Phys. Bull.* **2011**, *66*, 155–161. [CrossRef]
38. Li, J.; Zong, B.; Wang, Y.; Zhuang, W. Experiment and modeling of mechanical properties on iron matrix composites reinforced by different types of ceramic particles. *Mater. Sci. Eng. A* **2010**, *527*, 7545–7551. [CrossRef]
39. Dube, R.K. The extraction of lead from its ores by the iron-reduction process: A historical perspective. *JOM* **2006**, *58*, 18–23. [CrossRef]
40. Raghavan, V. Fe-Ti-Zr (Iron-Titanium-Zirconium). *J. Phase Equilibria Diffus.* **2010**, *31*, 469. [CrossRef]
41. Jiang, M.; Oikawa, K.; Ikeshoji, T.; Wulff, L.; Ishida, K. Thermodynamic calculations of Fe-Zr and Fe-Zr-C systems. *J. Phase Equilibria* **2001**, *22*, 406–417. [CrossRef]

42. Ali, K.; Arya, A.; Ghosh, P.; Dey, G. A first principles study of cohesive, elastic and electronic properties of binary Fe-Zr intermetallics. *Comput. Mater. Sci.* **2016**, *112*, 52–66. [CrossRef]
43. Liu, Y.; Allen, S.M.; Livingson, J.D. An investigation of Fe_3Zr phase. *Scr. Metall. Mater.* **1995**, *32*, 1129–1132. [CrossRef]
44. Zhou, G.; Zeng, D.; Liu, Z. Phase equilibria in the Fe-Ti-Zr system at 1023K. *J. Alloys Compd.* **2010**, *490*, 463–467. [CrossRef]
45. Arajs, S.; Colvin, R.V. Ferromagnetic-paramagnetic transition in iron. *J. Appl. Phys.* **1964**, *35*, 2424–2426. [CrossRef]
46. Maruno, W.; Morizono, Y.; Tsurekawa, S. Differential scanning calorimetry of the α/γ transformation in Fe-Co alloys under a magnetic field. *Mater. Trans.* **2013**, *54*, 1823–82013. [CrossRef]
47. Dumitrescu, L.F.S.; Hillert, M.; Sounders, N. Comparison of Fe-Ti assessments. *J. Phase Equilibria* **1998**, *19*, 441. [CrossRef]
48. Cao, X.; Jin, J.; Zhang, Y.; Zong, B.Y. Mechanical properties of iron matrix composites reinforced by copper-coated hybrid ceramic particles. *J. Mater. Res.* **2015**, *30*, 2360–2368. [CrossRef]